

A finite element implementation of a large deformation gradient-damage theory for fracture with Abaqus user material subroutines

Keven Alkhoury^{†*}, Shawn A. Chester[‡], and Vikas Srivastava^{†*}

[†] School of Engineering
Brown University
184 Hope Street, Providence, RI 02906 USA

[‡] Mechanical Engineering
New Jersey Institute of Technology
Newark, NJ 07102 USA

August 17, 2025

Abstract

Recent advancements in computations have enabled the application of various modeling approaches to predict fracture and failure, such as the gradient-damage (phase-field) method. Several existing studies have leveraged the heat equation solver in Abaqus to model gradient-damage, due to its mathematical resemblance to the heat equation. Particular care is required when extending the approach to large deformation scenarios due to differences in the *referential* and *spatial* configurations, especially since the heat equation in Abaqus is solved in the spatial configuration, whereas most gradient-damage frameworks are formulated in the referential configuration. This work provides a pedagogic view of an appropriate Abaqus implementation of a gradient-damage theory for fracture in materials *undergoing large deformation* using Abaqus UMAT and UMATHT user subroutines. Key benchmark problems from the literature are used to demonstrate the robustness of our implementation across various materials exhibiting different constitutive behaviors, such as non-linear elasticity, linear elasticity, and large deformation rate-dependent plasticity, ensuring its applicability regardless of the specific material constitutive choice. The details of the implementation, along with the codes, which are a direct outcome of this work, are also provided.

Keywords: Gradient-damage, Phase-field, Finite Element Method, Abaqus implementation, Large deformation, UMAT, UMATHT

*Corresponding authors: keven.alkhoury@brown.edu & vikas.srivastava@brown.edu

1 Introduction

Failure and fracture have long played a central role in shaping the world around us. From natural evolution to human engineering, the ability of materials and structures to resist breaking when subjected to loadings has been vital to survival, safety, and progress. Over the last century, rapid technological advancements have deepened our understanding of the mechanics of materials and sparked scientific interest in fracture mechanics, with groundbreaking development tracing back to Griffith (1921) whose work laid the foundation for the field.

The literature related to phase-field modeling of fracture, originally formulated to include quasi-static brittle settings (Francfort and Marigo, 1998; Bourdin et al., 2000; Miehe et al., 2010a,b), has seen significant theoretical development including dynamic fracture (Borden et al., 2012), ductile fracture (Ambati et al., 2015, 2016), as well as large deformation fracture, often encountered in polymeric materials (Miehe and Schänzel, 2014; Talamini et al., 2018; Narayan and Anand, 2021; Konale and Srivastava, 2025).

More recently, advancements in computation have enabled the application of various modeling approaches to predict fracture and failure, such as the gradient-damage (phase-field) method,¹ which is capable of modeling damage and failure in a wide range of materials, including metals (Miehe et al., 2015b; Chu et al., 2019), rubbers (Miehe and Schänzel, 2014; Talamini et al., 2018; Loew et al., 2019), glass (Mehrmashhadi et al., 2020; Egboiyi et al., 2022), ceramics (Wilson et al., 2013; Li et al., 2022), fiber-reinforced composites (Zhang et al., 2019; Konica and Sain, 2023). It also has the capability of predicting various multiphysics problems with a variety of failure mechanisms, such as hydrogen-embrittlement (Kristensen et al., 2020; Dinachandra and Alankar, 2022; Cui et al., 2022) and thermal degradation (Miehe et al., 2015a; Svolos et al., 2020; Najmeddine and Shakiba, 2024b), to name a few.

As a reminder, the phase-field method utilizes a scalar variable representing “damage” denoted as d and its gradient, ∇d , to regularize the sharp crack topology by introducing a diffusive damage zone within a characteristic length scale l . Some key advantages of this approach are resolving numerical challenges associated with sharp cracks and discontinuities and facilitating mesh-independent crack propagation simulations. Consequently, significant effort has been dedicated by the computational mechanics community to implementing the gradient-damage theory in both commercially available programs such as ABAQUS and COMSOL, and open-source programs such as FEniCS (cf. eg., Msekhe et al., 2015; Liu et al., 2016; Molnár and Gravouil, 2017; Zhou et al., 2018; Fang et al., 2019; Hirshikesh et al., 2019; Li and Bouklas, 2020; Molnár et al., 2020; Wu and Huang, 2020; Kristensen et al., 2020; Najmeddine and Shakiba, 2024a; Hai et al., 2024; George et al., 2025, and references within).

In what follows, we focus our attention on Abaqus due to its widespread popularity and extensive use within the mechanics community (Zhong and Srivastava, 2021; Navidtehrani et al., 2021a,b; Konale et al., 2023; Vaishakh et al., 2024). Notably, most existing studies utilizing Abaqus to model phase-field fracture have involved the use of multiple subroutines,

¹While the term “phase-field” can refer to a broader class of methods depending on the application (i.e., solidification, fracture, multi-phase systems, etc.), we use in this work the terms “gradient-damage” and “phase-field” interchangeably to describe the regularized formulation of damage evolution and fracture in solids.

often incorporating a user element (UEL) (Lee et al., 2023; Konale and Srivastava, 2025), which are complex to implement, or are restricted to linear constitutive behavior, i.e., small strain kinematics. The excellent contributions of Navidtehrani et al. (2021a,b) address the first limitation by providing a simple yet robust implementation using only a user material subroutine (UMAT). This eliminates the complexities of UEL programming and enables the use of Abaqus built-in features. However, their approach remains limited to brittle failure under small-strain kinematics and cannot capture the large-deformation fracture and failure behavior critical for predicting the response of many engineering materials.

The objective of this work is to address the shortcomings listed above by providing a pedagogic view of an appropriate Abaqus implementation of a gradient-damage theory for fracture in materials *undergoing large deformation* using Abaqus user material subroutines UMAT and UMATHHT.² This allows for accurately solving damage and failure problems without the need for writing complex UELs. We note that the intention of this work is not to develop a new damage framework but rather to implement existing theories efficiently and correctly, using Abaqus user material subroutines (reviewed and summarized in Section 2). We accomplish this by carefully reviewing the analogy between the heat equation implemented in Abaqus, and the partial differential equation (PDE) governing gradient-damage theory for large deformation fracture in Section 3. Next, we provide the detailed finite element implementation using the user material subroutines UMAT and UMATHHT (Abaqus/Standard, 2024), which was verified against the user element implementation provided by Lee et al. (2023) and applied to benchmark problems from the literature in Section 4, including a penny-shaped specimen in tension, a single edge notched tension (SENT) test, and a single edge notched beam (SENB) test. Lastly, we provide the Abaqus user material subroutines and the corresponding input files as supplemental materials to this paper.

2 Summary of the gradient-damage theory

In this section, we summarize the gradient-damage theory for solids undergoing large deformation following the existing work in literature (Miehe and Schänzel, 2014; Talamini et al., 2018; Narayan and Anand, 2021; Lee et al., 2023; Konale and Srivastava, 2025, and references within). For further details related to the theoretical framework, the reader is referred to the original works cited above.

2.1 Kinematics

Consider an undeformed body \mathcal{B}_R identified with the region of space it occupies in a fixed reference configuration, and denote by \mathbf{x}_R an arbitrary material point of \mathcal{B}_R . The referential body \mathcal{B}_R then undergoes a motion $\mathbf{x} = \boldsymbol{\chi}(\mathbf{x}_R, t)$ to the deformed body \mathcal{B}_t with deformation gradient given by³

$$\mathbf{F} = \nabla \boldsymbol{\chi}, \quad \text{such that} \quad J = \det \mathbf{F} > 0. \quad (1)$$

²As will be clarified shortly, the UMATHHT subroutine enables the modification of the thermal constitutive behavior and is essential for capturing the mechanics associated with large deformation kinematics, due to differences in the *referential* and *spatial* configurations.

³Following common notation (Gurtin et al., 2010), the symbols ∇ and Div denote the gradient and divergence with respect to the material point \mathbf{x}_R in the reference configuration; while grad and div denote

The right and left Cauchy-Green deformation tensors are given by

$$\mathbf{C} = \mathbf{F}^\top \mathbf{F}, \quad (2)$$

and

$$\mathbf{B} = \mathbf{F}\mathbf{F}^\top. \quad (3)$$

Also, the polar decomposition of the deformation gradient

$$\mathbf{F} = \mathbf{R}\mathbf{U} \quad (4)$$

allows its split into a rotation \mathbf{R} , and a symmetric stretch \mathbf{U} .

2.2 Free energy

Following recent literature, we introduce a scalar damage field $d \in [0, 1]$, which characterizes an intact (damage-free) state when $d = 0$ and a fully-damaged state when $d = 1$. Consequently, we introduce the degraded free energy density per unit reference volume due to damage evolution such that

$$\begin{aligned} \hat{\psi}_{\mathbf{R}} &= \hat{\psi}_{\mathbf{R}}(\mathbf{C}, d, \nabla d) \\ &= \hat{\psi}_{\mathbf{R}}^*(\mathbf{C}, d) + \hat{\psi}_{\mathbf{R}, \text{nonlocal}}(\nabla d), \end{aligned} \quad (5)$$

where $\hat{\psi}_{\mathbf{R}}^*$, $\hat{\psi}_{\mathbf{R}, \text{nonlocal}}$, and ∇d represent the degraded free energy, the nonlocal damage contribution of the free energy, and the *referential* gradient of damage defined by $\nabla d \stackrel{\text{def}}{=} \frac{\partial d}{\partial \mathbf{x}_{\mathbf{R}}}$, respectively. The degraded free energy is defined such that

$$\hat{\psi}_{\mathbf{R}}^* \stackrel{\text{def}}{=} g(d) \hat{\psi}_{\mathbf{R}}^0(\mathbf{C}), \quad (6)$$

where the monotonically decreasing degradation function $g(d)$ has the following properties

$$g'(d) \leq 0 \quad \text{with} \quad g(0) = 1, \quad g(1) = 0, \quad \text{and} \quad g'(1) = 0, \quad (7)$$

and is constitutively prescribed as

$$g(d) = (1 - d)^2, \quad (8)$$

and $\hat{\psi}_{\mathbf{R}}^0(\mathbf{C})$ is the free energy of the undamaged body. Next, the nonlocal damage contribution of the free energy is defined such that

$$\hat{\psi}_{\mathbf{R}, \text{nonlocal}}(\nabla d) \stackrel{\text{def}}{=} \frac{1}{2} \varepsilon_{\mathbf{R}}^f l^2 |\nabla d|^2, \quad (9)$$

where $\varepsilon_{\mathbf{R}}^f$ and l correspond to the fracture energy per unit reference volume and the intrinsic characteristic length scale for the damage process, respectively.

these operators with respect to the point $\mathbf{x} = \boldsymbol{\chi}(\mathbf{x}_{\mathbf{R}}, t)$ in the deformed configuration. Also, we write $\text{tr } \mathbf{A}$, $\text{sym } \mathbf{A}$, $\text{skw } \mathbf{A}$, and \mathbf{A}_0 respectively, for the trace, symmetric, skew, and deviatoric parts of a tensor \mathbf{A} . Lastly, the inner product of tensors \mathbf{A} and \mathbf{B} is denoted by $\mathbf{A} : \mathbf{B}$, and the magnitude \mathbf{A} by $|\mathbf{A}| = \sqrt{\mathbf{A} : \mathbf{A}}$.

2.3 Governing equations and boundary conditions in the referential configuration

2.3.1 Referential macroforce balance: Balance of forces and moments

As is standard, neglecting inertial effects, the balance of forces and moments in the reference body \mathcal{B}_R are expressed as

$$\operatorname{div} \mathbf{T}_R + \mathbf{b}_R = \mathbf{0} \quad \text{and} \quad \mathbf{T}_R \mathbf{F}^\top = \mathbf{F} \mathbf{T}_R^\top, \quad (10)$$

where \mathbf{T}_R and \mathbf{b}_R represent the Piola-Kirchhoff stress and an external body force per unit reference volume, respectively. Additionally, the standard boundary conditions are prescribed motion and tractions

$$\left. \begin{aligned} \boldsymbol{\chi} &= \check{\boldsymbol{\chi}} && \text{on } \mathcal{S}_{\check{\boldsymbol{\chi}}}, \\ \mathbf{T}_R \mathbf{n}_R &= \check{\mathbf{t}}_R && \text{on } \mathcal{S}_{\check{\mathbf{t}}_R}, \end{aligned} \right\} \quad (11)$$

where $\mathcal{S}_{\check{\boldsymbol{\chi}}}$ and $\mathcal{S}_{\check{\mathbf{t}}_R}$ represent complementary subsurfaces of the boundary $\partial \mathcal{B}_R$ of the body \mathcal{B}_R , such that $\partial \mathcal{B}_R = \mathcal{S}_{\check{\boldsymbol{\chi}}} \cup \mathcal{S}_{\check{\mathbf{t}}_R}$ and $\mathcal{S}_{\check{\boldsymbol{\chi}}} \cap \mathcal{S}_{\check{\mathbf{t}}_R} = \emptyset$, with an initial condition $\boldsymbol{\chi}(\mathbf{x}_R, \mathbf{0}) = \boldsymbol{\chi}_0(\mathbf{x}_R)$ in \mathcal{B}_R .

2.3.2 Referential microforce balance: Damage evolution equation

The balance of microforces in the reference body \mathcal{B}_R takes the form

$$\operatorname{Div} \boldsymbol{\xi}_R - \omega_R = 0, \quad (12)$$

where the scalar and vector microscopic stresses, ω_R and $\boldsymbol{\xi}_R$, conjugates to d and ∇d , respectively, are constitutively prescribed such that

$$\begin{aligned} \omega_R &= \frac{\partial \hat{\psi}_R^*}{\partial d} + \omega_{R,\text{diss}}, \quad \text{and} \\ \boldsymbol{\xi}_R &= \frac{\partial \hat{\psi}_{R,\text{nonlocal}}}{\partial \nabla d} = \varepsilon_R^f l^2 \nabla d. \end{aligned} \quad (13)$$

Moreover, the dissipative part of ω_R is given by

$$\omega_{R,\text{diss}} = \alpha + \zeta_R \dot{d}, \quad (14)$$

with α representing the dissipated fracture energy per unit reference volume during damage evolution such that $\alpha = \varepsilon_R^f d$, and ζ_R representing a viscous regularization parameter. Next, use of (8), (13) and (14) allow (12) to be recast such that

$$\zeta_R \dot{d} = 2(1-d) \hat{\psi}_R^0 + \varepsilon_R^f l^2 \operatorname{Div}(\nabla d) - \varepsilon_R^f d, \quad (15)$$

along with boundary conditions such that

$$\left. \begin{aligned} d &= 0 && \text{on } \mathcal{S}_d, \\ \nabla d \cdot \mathbf{n}_R &= 0 && \text{on } \mathcal{S}_{\boldsymbol{\xi}_R}, \end{aligned} \right\} \quad (16)$$

where \mathcal{S}_d and \mathcal{S}_{ξ_R} represent complementary subsurfaces of the boundary $\partial\mathcal{B}_R$ of the body \mathcal{B}_R , such that $\partial\mathcal{B}_R = \mathcal{S}_d \cup \mathcal{S}_{\xi_R}$ and $\mathcal{S}_d \cap \mathcal{S}_{\xi_R} = \emptyset$, with an initial condition $d(\mathbf{x}_R, 0) = 0$ in \mathcal{B}_R . Lastly, to enforce damage irreversibility ($\dot{d} > 0$), we introduce the monotonically increasing history function following Miehe et al. (2010a) such that

$$\mathcal{H}_R(t) = \max_{s \in [0, t]} \hat{\psi}_R^0(\mathbf{C}(s)), \quad (17)$$

which allows recasting (15) into

$$\zeta_R \dot{d} = 2(1 - d)\mathcal{H}_R - \varepsilon_R^f d + \varepsilon_R^f l^2 \text{Div}(\nabla d). \quad (18)$$

2.4 Governing equations and boundary conditions in the spatial configuration

2.4.1 Spatial macroforce balance: Balance of forces and moments

Once again, neglecting inertial effects, the balance of forces and moments in the deformed body \mathcal{B}_t are expressed as

$$\text{div} \mathbf{T} + \mathbf{b} = \mathbf{0} \quad \text{and} \quad \mathbf{T} = \mathbf{T}^\top, \quad (19)$$

where \mathbf{T} and \mathbf{b} represent the Cauchy stress and an external body force per unit deformed volume, respectively. Moreover, the standard boundary conditions are prescribed displacement and tractions

$$\left. \begin{array}{ll} \mathbf{u} = \check{\mathbf{u}} & \text{on } \mathcal{S}_{\check{\mathbf{u}}}, \\ \mathbf{T}\mathbf{n} = \check{\mathbf{t}} & \text{on } \mathcal{S}_{\check{\mathbf{t}}}, \end{array} \right\} \quad (20)$$

where $\mathcal{S}_{\check{\mathbf{u}}}$ and $\mathcal{S}_{\check{\mathbf{t}}}$ represent complementary subsurfaces of the boundary $\partial\mathcal{B}_t$ of the body \mathcal{B}_t , such that, $\partial\mathcal{B}_t = \mathcal{S}_{\check{\mathbf{u}}} \cup \mathcal{S}_{\check{\mathbf{t}}}$ and $\mathcal{S}_{\check{\mathbf{u}}} \cap \mathcal{S}_{\check{\mathbf{t}}} = \emptyset$, with an initial condition $\mathbf{u}(\mathbf{x}_R, 0) = \mathbf{u}_0(\mathbf{x}_R)$ in \mathcal{B}_R .

2.4.2 Spatial microforce balance: Damage evolution equation

The balance of microforces in the deformed body \mathcal{B}_t takes the form

$$\text{div} \boldsymbol{\xi} - \omega = 0, \quad (21)$$

where the scalar and vector microscopic stresses, ω and $\boldsymbol{\xi}$, conjugates to d and $\text{grad} d$, respectively, are related to their referential counterparts following

$$\left. \begin{array}{l} \omega = J^{-1} \omega_R, \quad \text{and} \\ \boldsymbol{\xi} = J^{-1} \mathbf{F} \boldsymbol{\xi}_R, \end{array} \right\} \quad (22)$$

which allows (13) to be recast such that

$$\left. \begin{array}{l} \omega = J^{-1} \frac{\partial \hat{\psi}_R^*}{\partial d} + \varepsilon^f d + \zeta \dot{d}, \quad \text{and} \\ \boldsymbol{\xi} = J^{-1} \varepsilon_R^f l^2 \mathbf{F} \mathbf{F}^\top \text{grad} d, \end{array} \right\} \quad (23)$$

with $\varepsilon^f = J^{-1} \varepsilon_R^f$ and $\zeta = J^{-1} \zeta_R$.

Next, use of (8), (17) and (23) allows (21) to be recast such that

$$\zeta \dot{d} = 2(1 - d)\mathcal{H} - \varepsilon^f d + \varepsilon_R^f l^2 \operatorname{div}(J^{-1} \mathbf{B} \operatorname{grad} d), \quad (24)$$

where the spatial history function is related to its referential counterpart using $\mathcal{H} = J^{-1} \mathcal{H}_R$. Lastly, the boundary conditions are given by

$$\left. \begin{array}{ll} d = 0 & \text{on } \mathcal{S}_d, \\ \operatorname{grad} d \cdot \mathbf{n} = 0 & \text{on } \mathcal{S}_\xi, \end{array} \right\} \quad (25)$$

where \mathcal{S}_d and \mathcal{S}_ξ represent complementary subsurfaces of the boundary $\partial \mathcal{B}_t$ of the body \mathcal{B}_t , such that, $\partial \mathcal{B}_t = \mathcal{S}_d \cup \mathcal{S}_\xi$ and $\mathcal{S}_d \cap \mathcal{S}_\xi = \emptyset$, with an initial condition $d(\mathbf{x}_R, 0) = 0$ in \mathcal{B}_R .

3 Finite element implementation

In this section, we explore the similarities between the heat equation and phase-field evolution by examining an Abaqus finite element implementation. We then comment on its validity and provide an Abaqus implementation of the gradient-damage theory for fracture in materials undergoing large deformation using user material subroutines UMAT and UMATHT.

3.1 Abaqus implementation: Analogy to the heat equation

As per the Abaqus documentation (Abaqus/Standard, 2024), the heat equation (energy balance) is given by

$$\int_V \rho \dot{U} dV = \int_S q dS + \int_V r dV, \quad (26)$$

where V is the volume of solid material with surface area S , ρ is the density of the material, \dot{U} is the material time rate of the internal thermal energy, q is the heat flux per unit area flowing into the body, and r is the heat supplied externally into the body per unit volume. Using the divergence theorem, along with Fourier’s law and the important relation $\dot{U} \stackrel{\text{def}}{=} C \dot{\theta}$, with C representing the specific heat measured in energy per unit mass per temperature for a fixed deformation, and $\dot{\theta}$ the rate of change of temperature, the heat equation (26) may be recast into its strong form

$$\rho C \dot{\theta} = \operatorname{div}(\mathbf{K} \operatorname{grad} \theta) + r, \quad (27)$$

where \mathbf{K} is the thermal conductivity tensor.

It is important to note here that Abaqus formulates the heat equation in the spatial (deformed) configuration in the sense that it uses spatial operators “div” rather than “Div” and “grad” rather than “∇”. This makes the damage evolution equation in the referential configuration (18) *fundamentally different* from the heat equation used in the Abaqus UMAT subroutine when dealing with large deformation kinematics. When applied within the *limits of small deformation* kinematics (i.e., brittle failure in linear elastic solids), since both referential and spatial operators are essentially the same, using the heat equation as provided in UMAT is an appropriate approximation.

Consequently, for an accurate implementation of the gradient-damage theory for fracture in materials undergoing large deformation using Abaqus user material subroutines, one needs to apply the analogy between the heat equation and the damage evolution equation in its spatial configuration, i.e., (24).

We start by recasting (24) such that

$$J^{-1}\zeta_{\text{R}}\dot{d} = \varepsilon_{\text{R}}^f l^2 \text{div}(J^{-1}\mathbf{B}\text{grad } d) + \underbrace{2(1-d)J^{-1}\mathcal{H}_{\text{R}} - J^{-1}\varepsilon_{\text{R}}^f d}_r, \quad (28)$$

and use it in Table 1 to show its resemblance to the heat equation using a term-by-term comparison.

Equation	Transient term	Conduction term	Source term
(27)	$\rho C \dot{\theta}$	$\text{div}(\mathbf{K}\text{grad } \theta)$	r
(28)	$J^{-1}\zeta_{\text{R}}\dot{d}$	$\varepsilon_{\text{R}}^f l^2 \text{div}(J^{-1}\mathbf{B}\text{grad } d)$	$2(1-d)J^{-1}\mathcal{H}_{\text{R}} - J^{-1}\varepsilon_{\text{R}}^f d$

Table 1: Term-by-term comparison of the heat equation (27) and the damage evolution equation (28).

In order to use the heat equation provided by Abaqus through the user subroutine UMAT, one needs to modify each of the terms in Table 1 as follows, with the caveat that the damage “ d ” is represented by temperature “ θ ”:

- Starting with the transient term, one needs to impose the equality $\rho C = J^{-1}\zeta_{\text{R}}$, which requires access to the thermal constitutive behavior that can be achieved using the user subroutine “UMATHHT.” The details are provided in Appendix A.1.
- Similarly, one needs to make two changes to the conduction term such that:
 1. The thermal conductivity tensor \mathbf{K} in Fourier’s law must be replaced by $J^{-1}\mathbf{B}$.
 2. The conduction term must be multiplied by a pre-factor $\varepsilon_{\text{R}}^f l^2$.

Both changes can be also done through the user subroutine “UMATHHT.” The details are provided in Appendix A.2.

- Lastly, the source term needs to be $r = 2(1-d)J^{-1}\mathcal{H}_{\text{R}} - J^{-1}\varepsilon_{\text{R}}^f d$, which can be directly achieved through the “RPL” functionality in the user subroutine “UMAT.” The details are provided in Appendix A.3.

3.2 Verification of implementation

In this section, we verify our proposed implementation in Abaqus/Standard (2024) by examining a series of simple boundary value problems, chosen to decouple each term as much as possible for detailed verification. We first study the homogeneous deformation of a rubber-like material subjected to large-stretch uniaxial tension at different stretch rates. This example serves to verify the coupled transient damage initiation/evolution only due to a source

term, without the presence of spatial gradients. We then study the inhomogeneous damage propagation in a rubber-like material in which we apply damage to a given geometry and allow it to propagate.⁴ This example serves to verify damage propagation throughout the material. In both examples, we compare our implementation using UMAT+UMATHHT against the UEL by Lee et al. (2023), where we adopt the slightly compressible Neo-Hookean material model with the constitutive details provided in Appendix B.1 for completeness.

3.2.1 Homogeneous damage initiation/evolution in a rubber-like material

In this example, we consider the plane strain homogeneous deformation in a rubber-like material subjected to a uniaxial tension at multiple stretch rates, as shown in Figure 1. Specifically, the reference body \mathcal{B}_R is a solid rectangle of initial dimension $L_0 = 0.01$ mm,

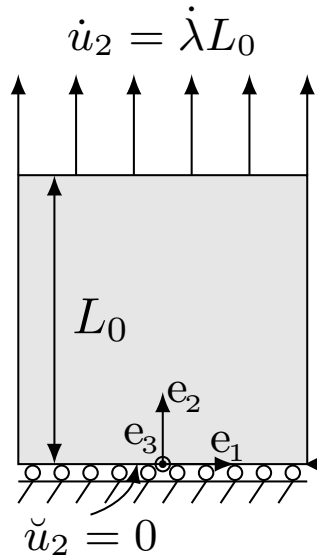


Figure 1: Schematic of the boundary value problem of a rubber-like material subjected to large-stretch uniaxial tension at different stretch rates.

with a roller boundary condition applied to its bottom surface, and its top surface subjected to a velocity (\dot{u}) boundary condition for various stretch rates ($\dot{\lambda}$), which can be achieved using the standard kinematic relation, $\dot{u} \stackrel{\text{def}}{=} \dot{\lambda} L_0$. Both the left and right sides are traction-free. Consequently, we modeled this problem using a single 4-node linear displacement-temperature plane strain element (CPE4T). For this boundary value problem, due to the spatial homogeneity, the only active component in the damage evolution equation, (28), is

⁴While this scenario may not reflect a typical boundary value problem, it provides a valuable and controlled setting to rigorously verify our implementation by isolating and analyzing individual contributions.

the source term “ r ” such that

$$J^{-1}\zeta_{\text{R}}\dot{d} = \underbrace{2(1-d)J^{-1}\mathcal{H}_{\text{R}} - J^{-1}\varepsilon_{\text{R}}^f d}_r. \quad (29)$$

Figures 2 and 3 compare the results of our implementation using Abaqus user material subroutines (UMAT+UMATHHT), and the user elements (UEL) by Lee et al. (2023).

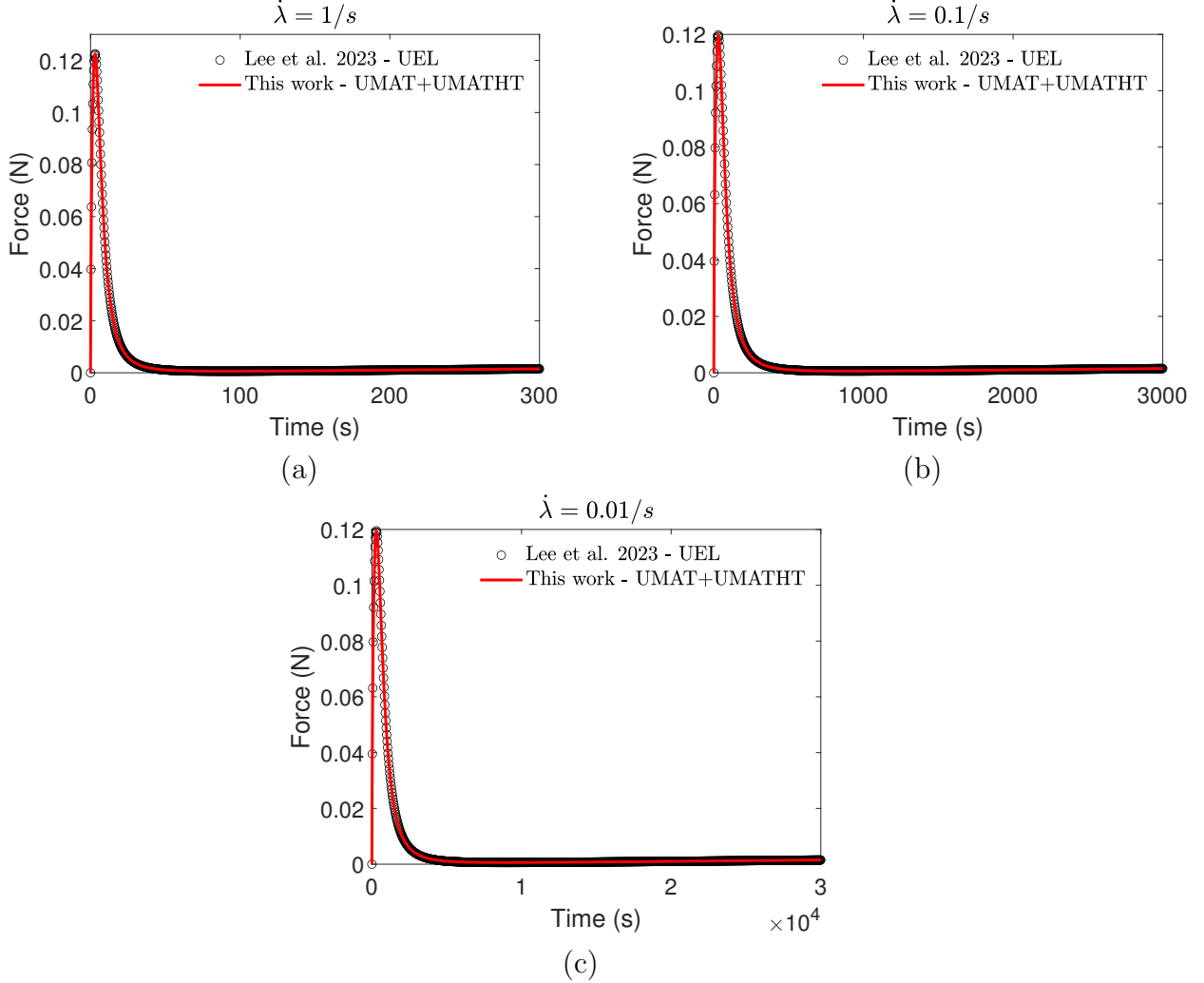


Figure 2: Comparison of the force-time response between the user element (UEL) by Lee et al. (2023) and Abaqus user material subroutines (UMAT+UMATHHT) developed in this work, at multiple stretch rates.

Specifically, Figure 2 shows the force-time response for multiple stretch rates, while Figure 3 shows the damage-time response, for multiple stretch rates. It can be observed from both Figures that our implementation here shows an identical response when compared to the results of the UEL by Lee et al. (2023), confirming the validity of the implementation in capturing the *transient* damage initiation and evolution due to a source term “ r ” as described in (29). We also observe slight variations in the response at different loading rates, which can be attributed to the rate-dependent nature of (29).

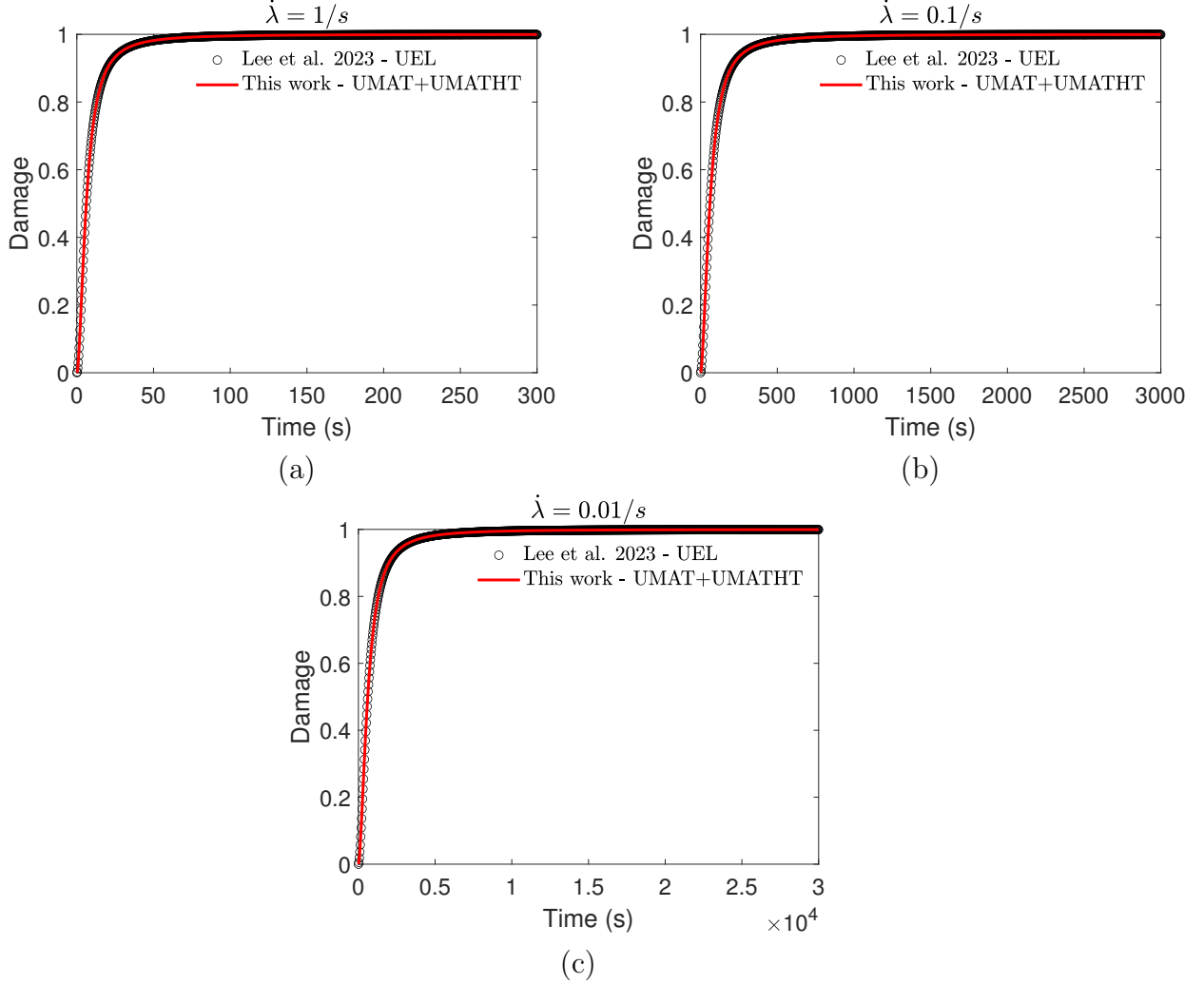


Figure 3: Comparison of the damage-time response between the user element (UEL) by Lee et al. (2023) and Abaqus user material subroutines (UMAT+UMATHHT) developed in this work, at multiple stretch rates.

3.2.2 Inhomogeneous damage propagation in a rubber-like material

In this example, we consider inhomogeneous damage propagation in a plane strain rubber-like material subjected to various boundary conditions. Specifically, we consider two scenarios:

- Scenario 1: We consider a fixed rectangular geometry with prescribed damage along the left and top sides. Specifically, the damage, d , is ramped linearly from 0 to 0.95 over 100 seconds, then remains fixed for another 200 seconds, allowing its propagation over a total of 300 seconds, as seen in Figure 4.
- Scenario 2: Two steps are considered in this scenario. In the first step, damage, d , is ramped linearly from 0 to 0.45 over 100 seconds along the left and top surfaces of the rectangle while it is fixed. In the second step, a displacement boundary condition is applied to its right (u_1) and bottom surfaces (u_2) simultaneously, ramped linearly

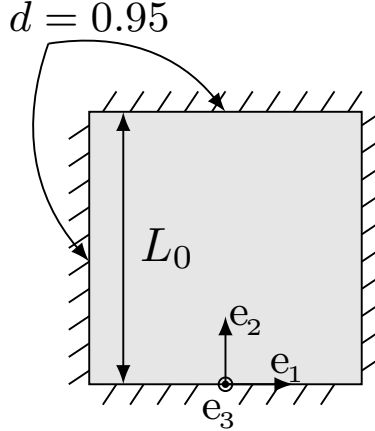


Figure 4: Schematic of the boundary value problem studied in Scenario 1, showing the inhomogeneous damage propagation in a fixed rubber-like material.

from 0 to 0.05 mm over 200 seconds, while the applied damage, d , applied in the first step is held constant throughout the entire step, as seen in Figure 5.

We note that the same geometry is used in the two scenarios, consisting of a reference body \mathcal{B}_R that is a solid rectangle of initial dimension $L_0 = 0.1$ mm, which was discretized using 10000 4-node linear displacement-temperature plane strain elements (CPE4T) with element size $l_e = 0.001$ mm.

Remark. Once again, we note that although these scenarios do not reflect typical boundary value problems, their simplicity provides a valuable and controlled setting to rigorously verify our implementation by isolating and analyzing individual contributions.

Scenario 1: Damage propagation in a fixed rectangular geometry

In this first scenario, since the body is fixed (i.e., $\mathbf{F} = \mathbf{1}$, $\mathbf{B} = \mathbf{1}$, and $J = 1$), the damage evolution equation (28) can be decoupled such that only the “conduction” term is active

$$\zeta_R \dot{d} = \varepsilon_R^f l^2 \operatorname{div}(\operatorname{grad} d). \quad (30)$$

Figure 6 shows the simulation results after 300 seconds, where we can see an excellent agreement between our implementation using UMAT+UMATHHT and the UEL by Lee et al. (2023). This confirms the validity of our UMAT+UMATHHT implementation in capturing the damage propagation due to “conduction” as described in (30). It is worth mentioning that although not shown here, this agreement was maintained throughout the entire simulation.

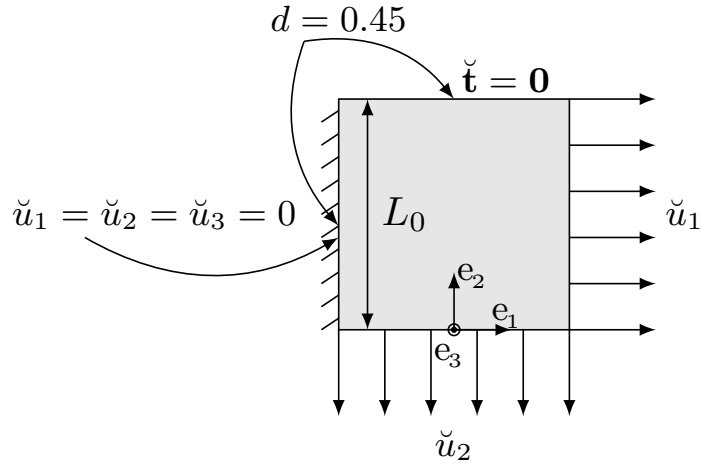


Figure 5: Schematic of the boundary value problem studied in Scenario 2, showing the inhomogeneous damage propagation in a deforming rubber-like material.

Scenario 2: Damage propagation in a deforming rectangular geometry

In the second scenario, the deforming body allows for testing the fully coupled damage evolution equation (28), verifying the robustness of our implementation. Similarly, Figure 7 shows the simulation results after 300 seconds, where we can see an excellent agreement between our implementation using UMAT+UMATHHT and the UEL by Lee et al. (2023). This confirms the validity of our implementation in capturing the fully coupled damage propagation in materials undergoing large deformation. Once again, this agreement was maintained throughout the entire simulation.

To summarize, following the results from Sections 3.2.1 and 3.2.2, we have verified our finite element implementation of a large deformation gradient-damage theory for fracture using Abaqus user material subroutines UMAT and UMATHHT, by comparing our implementation against the UEL by Lee et al. (2023). We use it in what follows to solve classical boundary value problems often encountered in the phase-field literature.

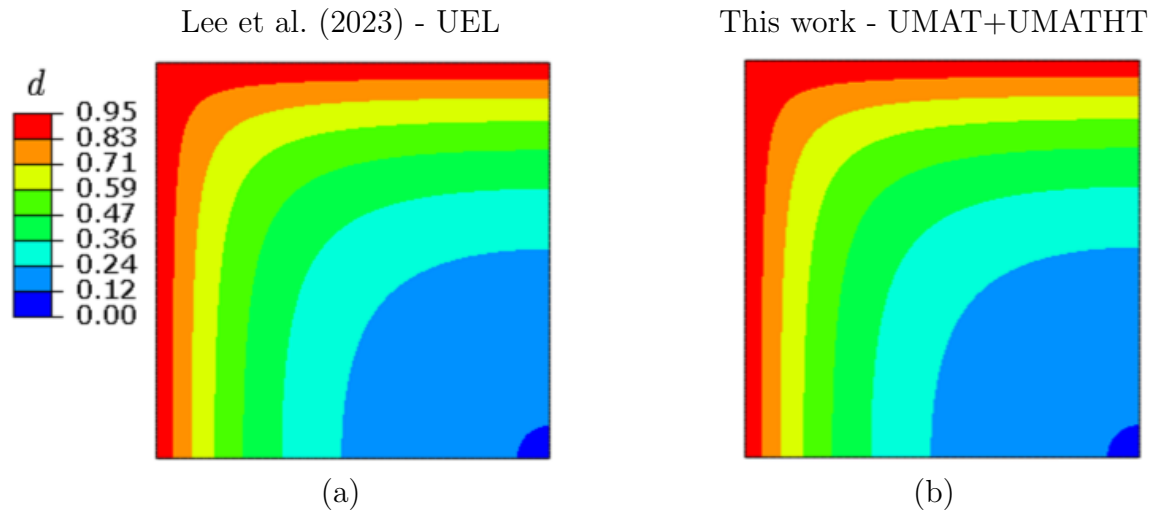


Figure 6: Comparison of the damage propagation in a fixed rectangular geometry between the user element (UEL) by Lee et al. (2023) and Abaqus user material subroutines (UMAT+UMATHHT) developed in this work.

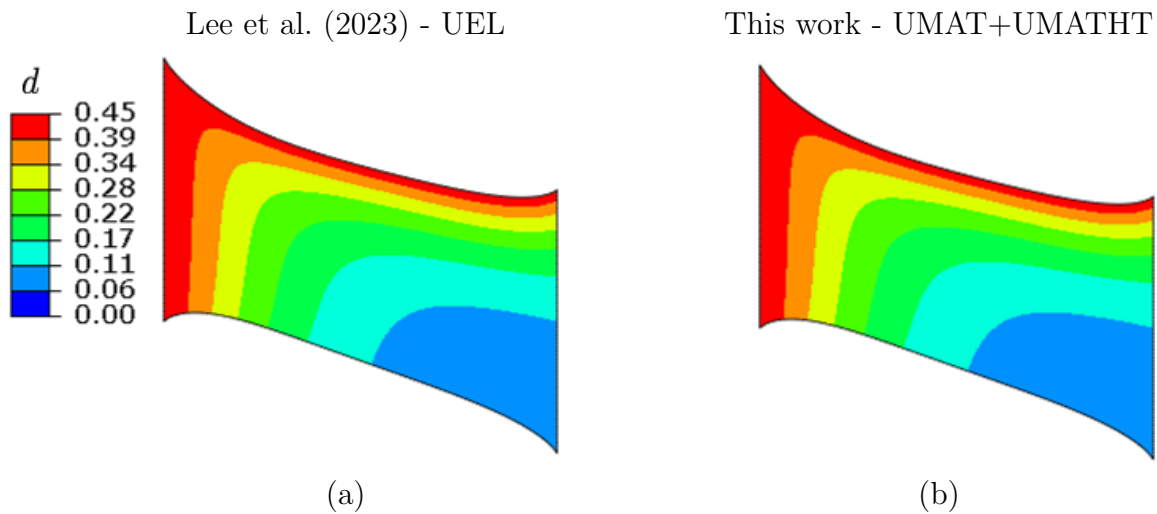


Figure 7: Comparison of the damage propagation in a deforming rectangular geometry between the user element (UEL) by Lee et al. (2023) and Abaqus user material subroutines (UMAT+UMATHHT) developed in this work.

4 Applications to fracture problems

In this section, we show the capabilities of our gradient-damage implementation for large deformation fracture using Abaqus user material subroutines UMAT and UMATHT. We validate it against key benchmark problems from the literature (Miehe et al., 2010a; Miehe and Schänzel, 2014). Specifically, we consider the following examples:

- Penny-shaped 3D specimen in tension utilizing a large deformation rubber material constitutive model.
- Single edge notched tension (SENT) test utilizing a small deformation linear elastic material constitutive model.
- Single edge notched beam (SENB) test utilizing a large deformation rate-dependent plasticity material constitutive model.

4.1 Penny-shaped specimen in tension: large deformation rubber

In this example, we examine the fracture response of a penny-shaped specimen with dimensions $L_0 = 2$ mm, $W_0 = 0.4$ mm, and $t_0 = 0.1$ mm. The specimen contains a pre-crack of length $a = 0.2$ mm at its center, as shown in Figure 8. The bottom surface is fixed, and

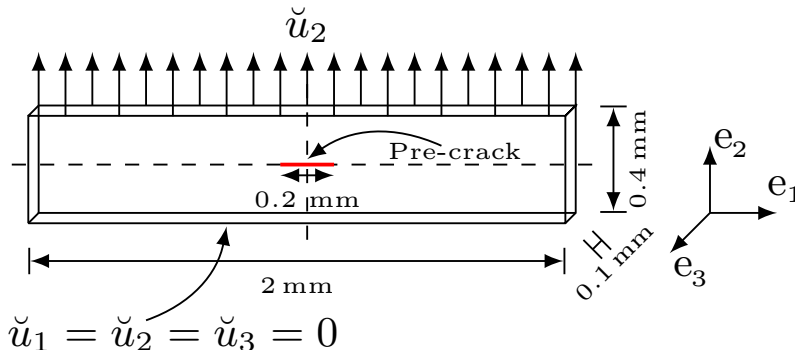


Figure 8: Schematic showing the geometry and boundary conditions for the penny-shaped specimen in tension.

displacement is applied to its top surface, such that u_2 increases linearly to 0.64 mm over 1600 seconds. All other surfaces are traction-free. The material constitutive response is taken as a compressible Neo-Hookean solid, with constitutive details and material parameters provided in Appendix B.1. Due to the symmetry, we only simulate one-eighth of the geometry. Specifically, the mesh consists of 6906 8-node linear displacement-temperature elements (C3D8T) with 2 elements through the (half-)thickness, with the elements near the pre-crack path having a mesh size $l_e = 0.005$ mm. Additionally, we use the UEL provided by Lee et al. (2023) to simulate the same boundary value problem for direct comparison.

It can be observed from Figure 9 that the force-displacement response is in excellent agreement between our implementation and the UEL by Lee et al. (2023). Moreover, Figure

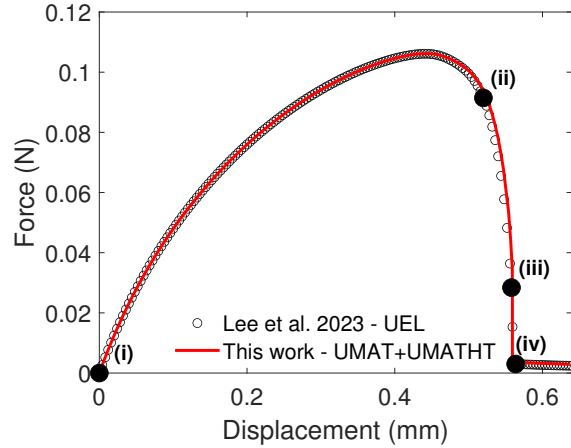


Figure 9: Comparison of the force-displacement results for the penny-shaped specimen in tension between the user element (UEL) by Lee et al. (2023) and Abaqus user material subroutines (UMAT+UMATHHT) developed in this work.

10 shows the damage evolution over time. The fracture initiates near the pre-crack and is propagated through the specimen until complete rupture, similar to what was reported in Lee et al. (2023). This benchmark problem proves the validity of the implementation developed in this work using UMAT+UMATHHT in predicting the fracture response in materials undergoing large deformation.

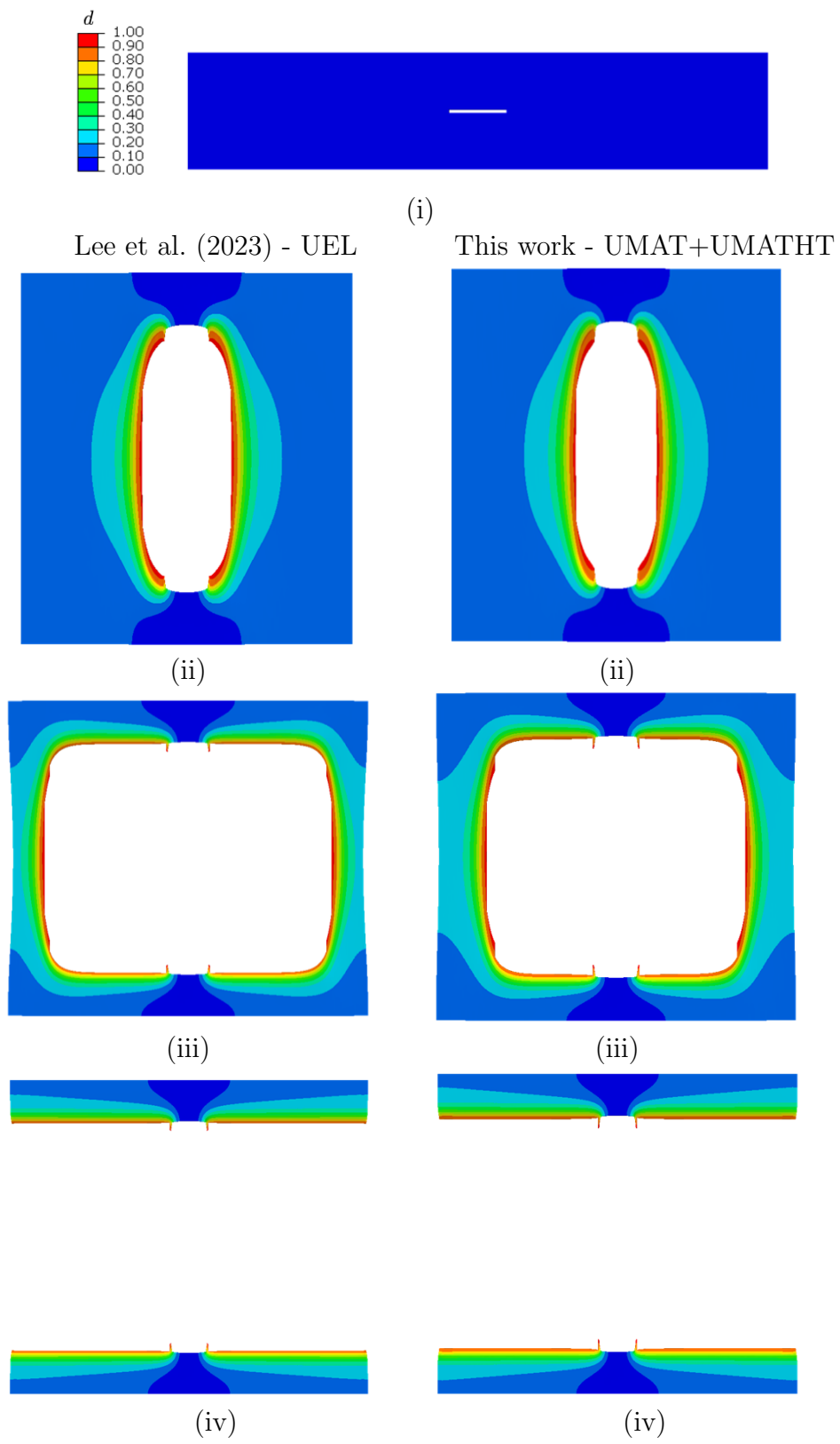


Figure 10: Comparison of the damage propagation for the penny-shaped specimen in tension between the user element (UEL) by Lee et al. (2023) and Abaqus user material subroutines (UMAT+UMATHHT) developed in this work at different instants shown in Figure 9. Note that the elements are not shown for $d > 0.95$.

4.2 Single edge notched tension test: small deformation linear elasticity

In this second example, we examine the fracture response of a single edge notched square plate of edge length $L_0 = 1$ mm, with a horizontal notch at mid-height, extending from the left outer surface to the center of the specimen, as shown in Figure 11. The bottom surface

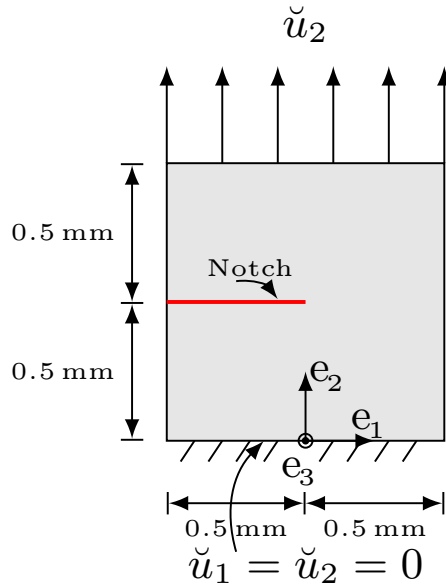


Figure 11: Schematic showing the geometry and boundary conditions for the single edge notched tension specimen.

is fixed, and displacement is applied to its top surface, such that u_2 increases linearly to 0.0035 mm over 100 seconds, resulting in a Mode I fracture. All other surfaces are traction-free. The material constitutive response is taken as a linear elastic solid, with details and material parameters provided in Appendix B.2. We model this problem using the plane strain approximation. Specifically, the mesh consists of 5289 4-node linear displacement-temperature elements (CPE4T), with the elements along the notch path having a mesh size $l_e = 0.005$ mm.

It can be observed from Figure 12 that upon reaching a critical energy value, there is a sharp drop in the force-displacement response resulting in a brittle fracture, similar to what was reported in Miehe et al. (2010b). Given the geometry and applied boundary conditions, the fracture initiates near the left notch and propagates instantaneously through the specimen, leading to brittle failure, as expected and shown in Figure 13. This benchmark problem again validates our implementation of the gradient-damage theory for large deformation, which was developed in this work using Abaqus user material subroutines. It also demonstrates that the implementation, while formulated for large deformation kinematics as the most general case, remains applicable within the limits of small deformation kinematics.

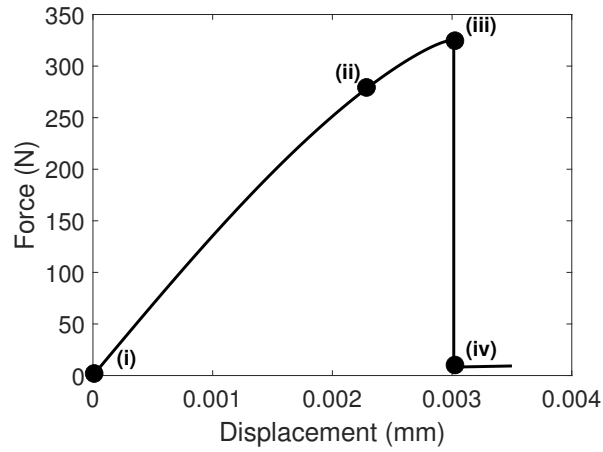


Figure 12: Force-displacement results for the SENT using Abaqus user material subroutines (UMAT+UMATHHT) developed in this work.

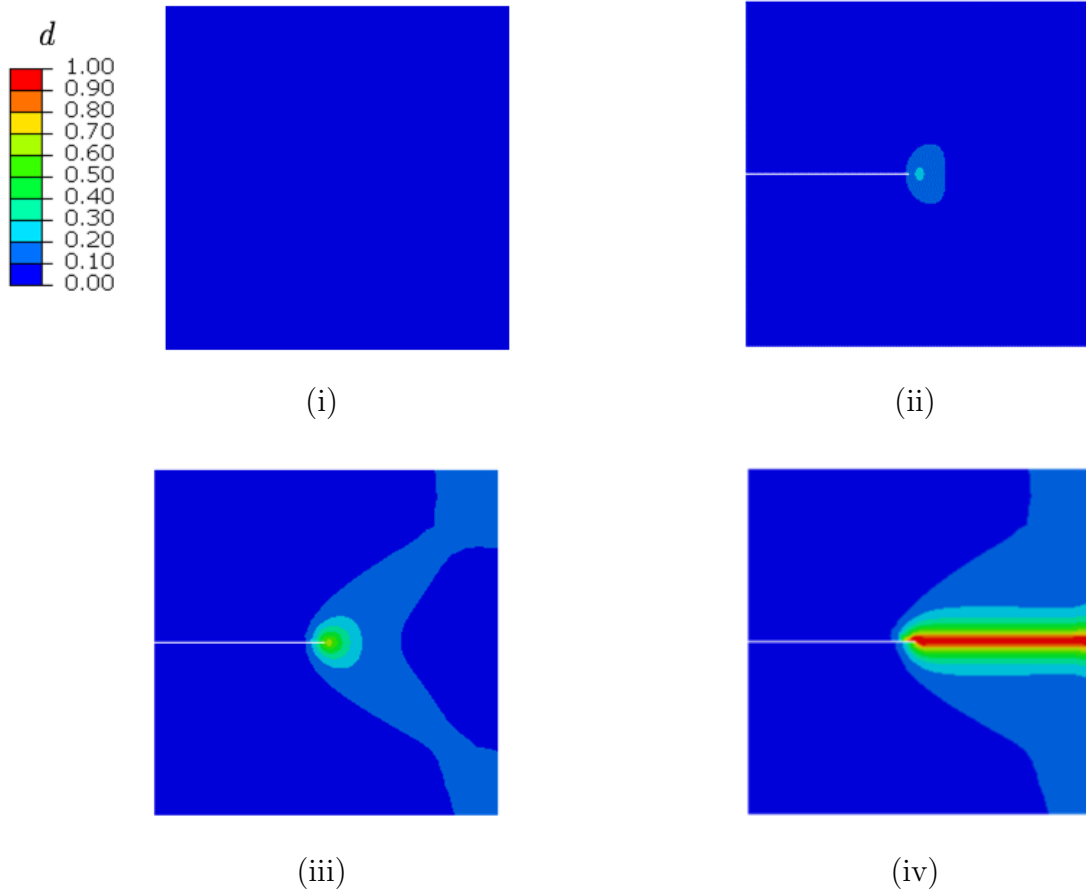


Figure 13: Damage evolution for the SENT test using Abaqus user material subroutines (UMAT+UMATHHT) developed in this work at different instants shown in Figure 12.

4.3 Single edge notched beam (SENB) test: large deformation rate-dependent plasticity

In this last example, we examine the fracture response of a single edge notched beam of length $L_0 = 10$ mm, and width $W_0 = 3$ mm with a vertical notch of size $a = 0.5$ mm, extending from the bottom-mid outer surface, as shown in Figure 14. The bottom left and right

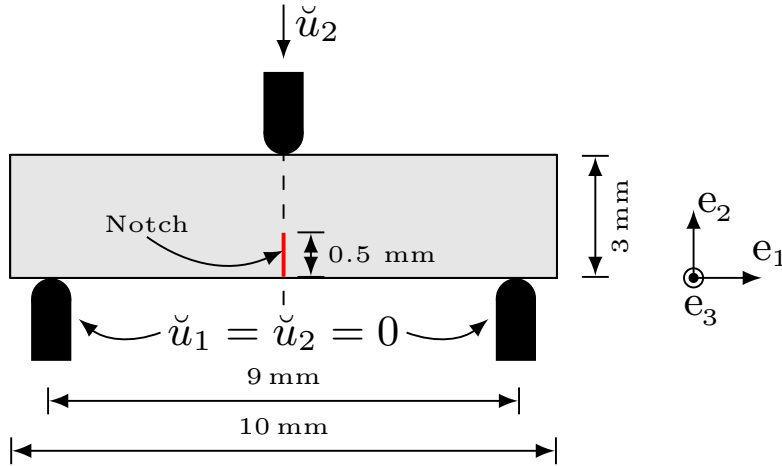


Figure 14: Schematic showing the geometry and boundary conditions for the single edge notched beam.

supports are fixed, and displacement is applied to its top support, such that u_2 is prescribed as seen in Figure 15a. Frictional contact with a friction coefficient of 0.3 is assumed to model the interaction between the support and the beam. All other surfaces are traction-free. In this example, the material constitutive response is taken to follow an isotropic rate-dependent elastic-plastic solid undergoing large deformation, with constitutive details and material parameters provided in Appendix B.3. We model this problem using a plane strain approximation. Specifically, the mesh consists of 17122 4-node linear displacement-temperature elements (CPE4T), with the elements along the notch path having a mesh size $l_e = 0.02$ mm.

It can be observed from Figure 15 that upon the first loading cycle, i.e., loading from (i) to (ii) and unloading from (ii) to (iii), the material undergoes some permanent deformation that can be observed upon partial unloading and is attributed to plasticity. We note that in this first loading cycle, the energy captured by the history function \mathcal{H}_R and shown in Figure 16b remains below its critical value near the notch and thus no damage is observed to that region (see Figure 17b). Moving onto the second loading cycle, i.e., loading from (iii) to (iv), the material is reloaded elastically until it reaches its prior maximum loading state, after which, it starts deforming plastically again. Upon further loading from (iv) to (v), the energy reaches and exceeds its critical value near the notch as can be observed in Figures 16c and d. Specifically, the damage nucleates near the notch on the bottom center and is quickly propagated through the specimen, causing a brittle failure captured by the force-displacement response and observed in Figures 17c and d.

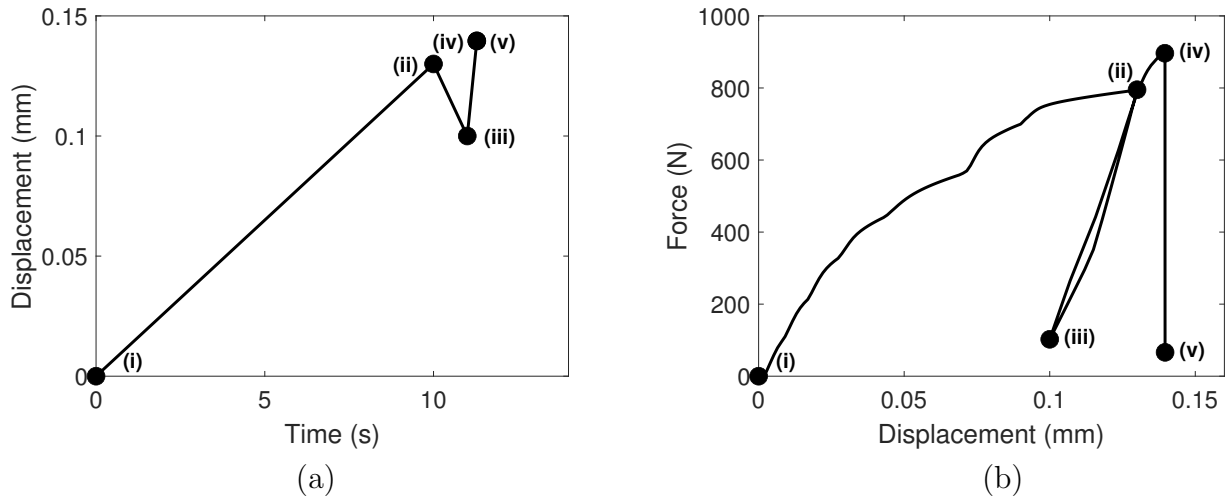


Figure 15: SENB results using Abaqus user material subroutines (UMAT+UMATHHT) developed in this work. (a) Prescribed displacement profile and (b) corresponding Force-displacement curve.

This final benchmark problem further demonstrates the robustness and versatility of our implementation, highlighting its applicability across a wide range of materials, ranging from nonlinear elasticity to large deformation rate-dependent plasticity, making it valuable to engineers in various disciplines.

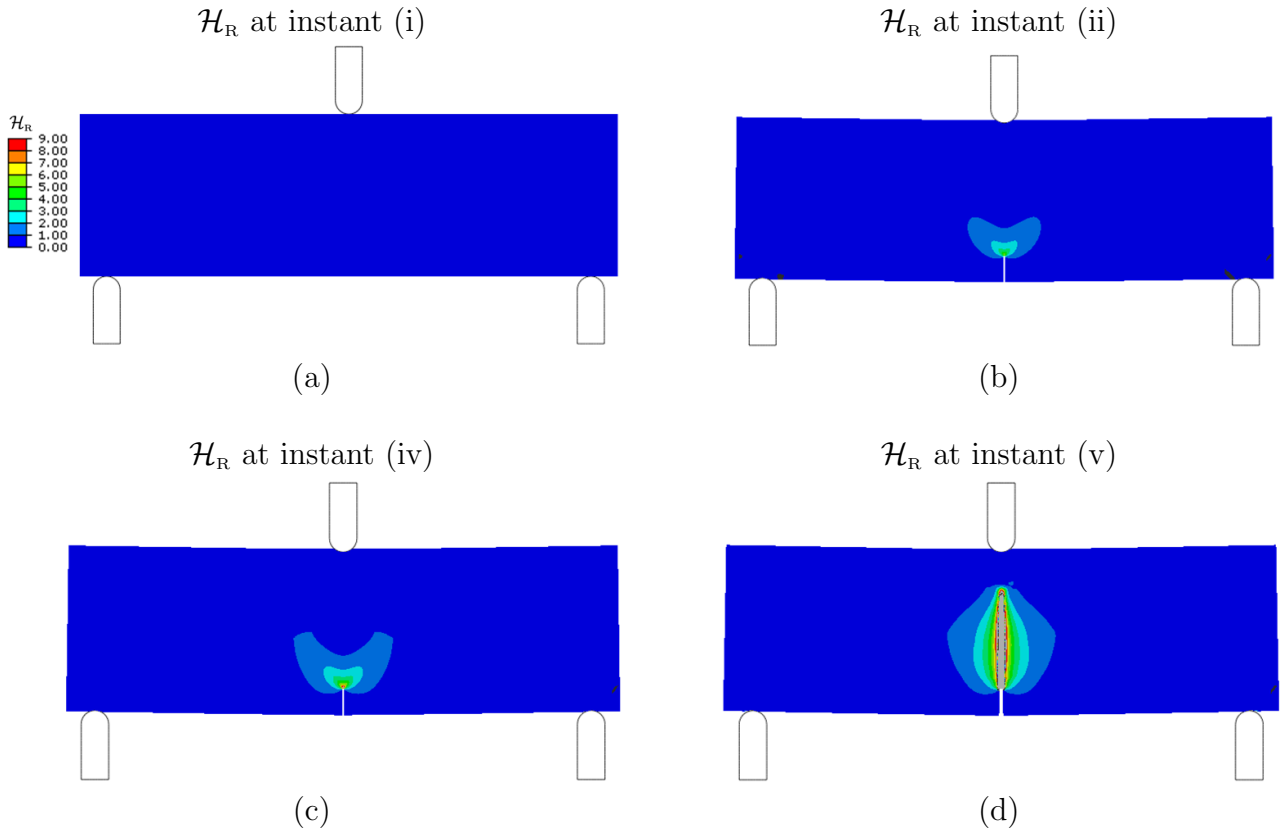


Figure 16: History function (\mathcal{H}_R) evolution for the SENB test using Abaqus user material subroutines (UMAT+UMATHHT) developed in this work at different instants shown in Figure 15. Note that the gray contour indicates regions where the values of \mathcal{H}_R exceed the limits shown in the legend.

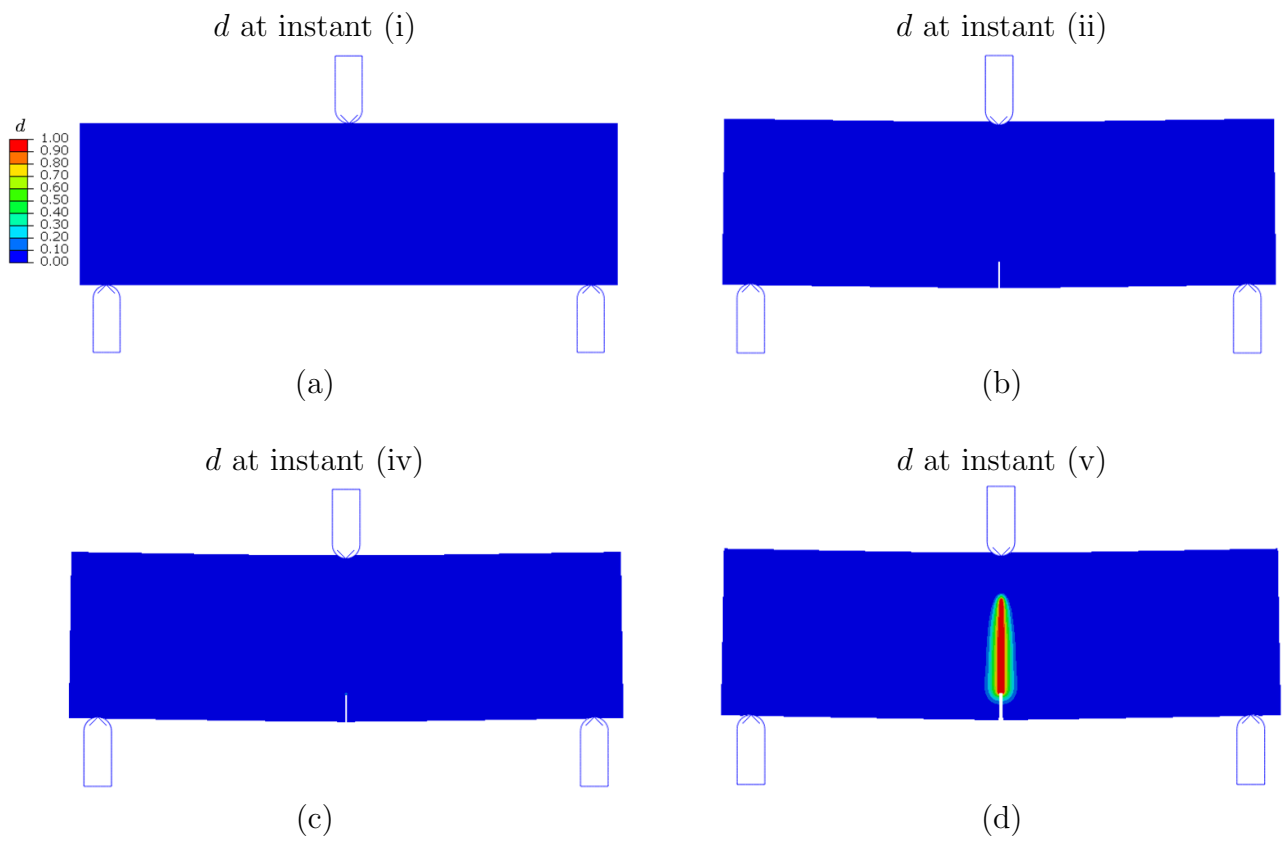


Figure 17: Damage (d) evolution for the SENB test using Abaqus user material subroutines (UMAT+UMATHHT) developed in this work at different instants shown in Figure 15.

5 Conclusion

In this work, we have provided a pedagogic view of an appropriate Abaqus implementation of a gradient-damage theory for fracture in materials undergoing large deformation using Abaqus user material subroutines UMAT and UMATHT, which allows for accurately solving damage and failure problems without the need for writing complex UELs.

This was accomplished by carefully reviewing the analogy between the heat equation implemented in Abaqus and the PDE governing the gradient-damage theory in the context of *large deformation*. The details of the implementation using the user material subroutines UMAT and UMATHT (Abaqus/Standard, 2024) were provided and validated against a user element implementation from (Lee et al., 2023). The UMAT and UMATHT implementation was further used to study classical benchmark problems from the literature, highlighting its robustness.

The Abaqus user material subroutines developed in this work and the input files are provided as supplemental materials to this paper. The implementation method and files provide researchers in the field with a simple yet robust tool to simulate and predict fracture and failure in solids, applicable to a broad class of materials through user-defined constitutive response.

CRediT authorship contribution statement

Keven Alkhoury: Conceptualization, Methodology, Software, Formal analysis, Investigation, Writing - Original Draft. **Shawn A. Chester:** Conceptualization, Writing - Review & Editing. **Vikas Srivastava:** Conceptualization, Supervision, Writing - Review & Editing, Funding acquisition.

Acknowledgments

KA acknowledges support from the Hibbitt Engineering Fellowship at Brown University. VS acknowledges support from the US Office of Naval Research under grant number N00014-21-1-2815. SAC acknowledges partial support from the National Science Foundation, USA under grant number CMMI-1751520. The opinions, findings, conclusions, and recommendations expressed are those of the authors and do not necessarily reflect the views of the National Science Foundation or any US government agencies.

Code availability

The code developed and used in this study will be made available upon publication.

References

- Abaqus/Standard. *Abaqus Reference Manuals*. Dassaults Systemes Simulia, Providence, RI, 2024.
- M. Ambati, T. Gerasimov, and L. De Lorenzis. Phase-field modeling of ductile fracture. *Computational Mechanics*, 55:1017–1040, 2015.
- M. Ambati, R. Kruse, and L. De Lorenzis. A phase-field model for ductile fracture at finite strains and its experimental verification. *Computational Mechanics*, 57:149–167, 2016.
- H. Amor, J.-J. Marigo, and C. Maurini. Regularized formulation of the variational brittle fracture with unilateral contact: Numerical experiments. *Journal of the Mechanics and Physics of Solids*, 57(8):1209–1229, 2009.
- L. Anand, N. M. Ames, V. Srivastava, and S. A. Chester. A thermo-mechanically coupled theory for large deformations of amorphous polymers. Part I: Formulation. *Int. J. Plast.*, 25(8):1474–1494, aug 2009. ISSN 0749-6419.
- M. J. Borden, C. V. Verhoosel, M. A. Scott, T. J. Hughes, and C. M. Landis. A phase-field description of dynamic brittle fracture. *Computer Methods in Applied Mechanics and Engineering*, 217:77–95, 2012.
- B. Bourdin, G. A. Francfort, and J.-J. Marigo. Numerical experiments in revisited brittle fracture. *Journal of the Mechanics and Physics of Solids*, 48(4):797–826, 2000.
- D. Chu, X. Li, Z. Liu, J. Cheng, T. Wang, Z. Li, and Z. Zhuang. A unified phase field damage model for modeling the brittle-ductile dynamic failure mode transition in metals. *Engineering Fracture Mechanics*, 212:197–209, 2019.
- C. Cui, R. Ma, and E. Martínez-Pañeda. A generalised, multi-phase-field theory for dissolution-driven stress corrosion cracking and hydrogen embrittlement. *Journal of the Mechanics and Physics of Solids*, 166:104951, 2022.
- M. Dinachandra and A. Alankar. Adaptive finite element modeling of phase-field fracture driven by hydrogen embrittlement. *Computer Methods in Applied Mechanics and Engineering*, 391:114509, 2022.
- B. Egboiyi, R. Matthey, S. Konica, P. Nikam, S. Ghosh, and T. Sain. Mechanistic understanding of the fracture toughening in chemically strengthened glass—experiments and phase-field fracture modeling. *International Journal of Solids and Structures*, 238:111374, 2022.
- J. Fang, C. Wu, T. Rabczuk, C. Wu, C. Ma, G. Sun, and Q. Li. Phase field fracture in elasto-plastic solids: Abaqus implementation and case studies. *Theoretical and Applied Fracture Mechanics*, 103:102252, 2019.
- G. A. Francfort and J.-J. Marigo. Revisiting brittle fracture as an energy minimization problem. *Journal of the Mechanics and Physics of Solids*, 46(8):1319–1342, 1998.

- D. George, S. Konica, I. Masters, and M. Hossain. A phase field formulation for modelling fracture of nearly incompressible hyperelastic materials. *Computer Methods in Applied Mechanics and Engineering*, 436:117696, 2025.
- A. A. Griffith. Vi. the phenomena of rupture and flow in solids. *Philosophical transactions of the royal society of london. Series A, containing papers of a mathematical or physical character*, 221(582-593):163–198, 1921.
- M. E. Gurtin, E. Fried, and L. Anand. *The mechanics and thermodynamics of continua*. Cambridge University Press, 2010.
- L. Hai, P. Wriggers, Y.-j. Huang, H. Zhang, and S.-l. Xu. Dynamic fracture investigation of concrete by a rate-dependent explicit phase field model integrating viscoelasticity and micro-viscosity. *Computer Methods in Applied Mechanics and Engineering*, 418:116540, 2024.
- Hirshikesh, S. Natarajan, and R. K. Annabattula. A fenics implementation of the phase field method for quasi-static brittle fracture. *Frontiers of Structural and Civil Engineering*, 13: 380–396, 2019.
- A. Konale and V. Srivastava. On modeling fracture of soft polymers. *Mechanics of Materials*, 206:105346, 2025.
- A. Konale, Z. Ahmed, P. Wanchoo, and V. Srivastava. A large deformation model for quasi-static to high strain rate response of a rate-stiffening soft polymer. *International Journal of Plasticity*, 168:103701, 2023.
- S. Konica and T. Sain. Phase-field fracture modeling for unidirectional fiber-reinforced polymer composites. *European Journal of Mechanics-A/Solids*, 100:105035, 2023.
- P. K. Kristensen, C. F. Niordson, and E. Martínez-Pañeda. A phase field model for elastic-gradient-plastic solids undergoing hydrogen embrittlement. *Journal of the Mechanics and Physics of Solids*, 143:104093, 2020.
- J. Lee, S. Lee, S. A. Chester, and H. Cho. Finite element implementation of a gradient-damage theory for fracture in elastomeric materials. *International Journal of Solids and Structures*, 279:112309, 2023.
- B. Li and N. Bouklas. A variational phase-field model for brittle fracture in polydisperse elastomer networks. *International Journal of Solids and Structures*, 182:193–204, 2020.
- D. Li, P. Li, W. Li, W. Li, and K. Zhou. Three-dimensional phase-field modeling of temperature-dependent thermal shock-induced fracture in ceramic materials. *Engineering Fracture Mechanics*, 268:108444, 2022.
- G. Liu, Q. Li, M. A. Msekh, and Z. Zuo. Abaqus implementation of monolithic and staggered schemes for quasi-static and dynamic fracture phase-field model. *Computational Materials Science*, 121:35–47, 2016.

- P. J. Loew, B. Peters, and L. A. Beex. Rate-dependent phase-field damage modeling of rubber and its experimental parameter identification. *Journal of the Mechanics and Physics of Solids*, 127:266–294, 2019.
- J. Mehrmashhadi, M. Bahadori, and F. Bobaru. On validating peridynamic models and a phase-field model for dynamic brittle fracture in glass. *Engineering Fracture Mechanics*, 240:107355, 2020.
- C. Miehe and L.-M. Schänzel. Phase field modeling of fracture in rubbery polymers. part i: Finite elasticity coupled with brittle failure. *Journal of the Mechanics and Physics of Solids*, 65:93–113, 2014.
- C. Miehe, M. Hofacker, and F. Welschinger. A phase field model for rate-independent crack propagation: Robust algorithmic implementation based on operator splits. *Computer Methods in Applied Mechanics and Engineering*, 199(45-48):2765–2778, 2010a.
- C. Miehe, F. Welschinger, and M. Hofacker. Thermodynamically consistent phase-field models of fracture: Variational principles and multi-field fe implementations. *International journal for numerical methods in engineering*, 83(10):1273–1311, 2010b.
- C. Miehe, M. Hofacker, L.-M. Schänzel, and F. Aldakheel. Phase field modeling of fracture in multi-physics problems. part ii. coupled brittle-to-ductile failure criteria and crack propagation in thermo-elastic–plastic solids. *Computer Methods in Applied Mechanics and Engineering*, 294:486–522, 2015a.
- C. Miehe, L.-M. Schänzel, and H. Ulmer. Phase field modeling of fracture in multi-physics problems. part i. balance of crack surface and failure criteria for brittle crack propagation in thermo-elastic solids. *Computer Methods in Applied Mechanics and Engineering*, 294:449–485, 2015b.
- G. Molnár and A. Gravouil. 2d and 3d abaqus implementation of a robust staggered phase-field solution for modeling brittle fracture. *Finite Elements in Analysis and Design*, 130:27–38, 2017.
- G. Molnár, A. Gravouil, R. Seghir, and J. Réthoré. An open-source abaqus implementation of the phase-field method to study the effect of plasticity on the instantaneous fracture toughness in dynamic crack propagation. *Computer Methods in Applied Mechanics and Engineering*, 365:113004, 2020.
- M. A. Msekh, J. M. Sargado, M. Jamshidian, P. M. Areias, and T. Rabczuk. Abaqus implementation of phase-field model for brittle fracture. *Computational Materials Science*, 96:472–484, 2015.
- A. Najmeddine and M. Shakiba. Efficient bfgs quasi-newton method for large deformation phase-field modeling of fracture in hyperelastic materials. *Engineering Fracture Mechanics*, 310:110463, 2024a.

- A. Najmeddine and M. Shakiba. Physics and chemistry-based phase-field constitutive framework for thermo-chemically aged elastomer. *International Journal of Mechanical Sciences*, 262:108721, 2024b.
- S. Narayan and L. Anand. Fracture of amorphous polymers: A gradient-damage theory. *Journal of the Mechanics and Physics of Solids*, 146:104164, 2021.
- Y. Navidtehrani, C. Betegón, and E. Martínez-Pañeda. A simple and robust abaqus implementation of the phase field fracture method. *Applications in Engineering Science*, 6:100050, 2021a.
- Y. Navidtehrani, C. Betegón, and E. Martinez-Paneda. A unified abaqus implementation of the phase field fracture method using only a user material subroutine. *Materials*, 14(8):1913, 2021b.
- V. Srivastava, S. A. Chester, N. M. Ames, and L. Anand. A thermo-mechanically-coupled large-deformation theory for amorphous polymers in a temperature range which spans their glass transition. *Int. J. Plast.*, 26(8):1138–1182, aug 2010. ISSN 0749-6419.
- L. Svolos, C. A. Bronkhorst, and H. Waisman. Thermal-conductivity degradation across cracks in coupled thermo-mechanical systems modeled by the phase-field fracture method. *Journal of the Mechanics and Physics of Solids*, 137:103861, 2020.
- B. Talamini, Y. Mao, and L. Anand. Progressive damage and rupture in polymers. *Journal of the Mechanics and Physics of Solids*, 111:434–457, 2018.
- K. Vaishakh, N. Parambil, and V. Srivastava. Hygroscopic damage of fiber–matrix interface in unidirectional composites: A computational approach. *International Journal of Mechanical Sciences*, 279:109460, 2024.
- Z. A. Wilson, M. J. Borden, and C. M. Landis. A phase-field model for fracture in piezoelectric ceramics. *International Journal of Fracture*, 183:135–153, 2013.
- J.-Y. Wu and Y. Huang. Comprehensive implementations of phase-field damage models in abaqus. *Theoretical and Applied Fracture Mechanics*, 106:102440, 2020.
- P. Zhang, X. Hu, T. Q. Bui, and W. Yao. Phase field modeling of fracture in fiber reinforced composite laminate. *International Journal of Mechanical Sciences*, 161:105008, 2019.
- J. Zhong and V. Srivastava. A higher-order morphoelastic beam model for tubes and filaments subjected to biological growth. *International Journal of Solids and Structures*, 233:111235, 2021.
- S. Zhou, T. Rabczuk, and X. Zhuang. Phase field modeling of quasi-static and dynamic crack propagation: Comsol implementation and case studies. *Advances in Engineering Software*, 122:31–49, 2018.

A Abaqus implementation using user material subroutines UMAT and UMATHT

In this appendix, we provide the details of the Abaqus implementation of the gradient-damage theory for large deformation fracture using user material subroutines UMAT and UMATHT.

Once again, to use the heat equation provided by Abaqus through the user subroutine UMAT, one needs to modify each of the terms in Table 1 (reproduced here for easier reading) as follows, with the caveat that the damage “ d ” is represented by temperature “ θ ”:

Equation	Transient term	Conduction term	Source term
(27)	$\rho C \dot{\theta}$	$\text{div}(\mathbf{K} \text{grad } \theta)$	r
(28)	$J^{-1} \zeta_{\text{R}} \dot{d}$	$\varepsilon_{\text{R}}^f l^2 \text{div}(J^{-1} \mathbf{B} \text{grad } d)$	$2(1-d)J^{-1} \mathcal{H}_{\text{R}} - J^{-1} \varepsilon_{\text{R}}^f d$

Table 1: Term-by-term comparison of the heat equation (27) and the damage evolution equation (28).

- Starting with the transient term, one needs to impose the equality $\rho C = J^{-1} \zeta_{\text{R}}$, which requires access to the thermal constitutive behavior that can be achieved using the user subroutine “UMATHT.”
- Similarly, one needs to make two changes to the conduction term such that:
 1. The thermal conductivity tensor \mathbf{K} in Fourier’s law must be replaced by $J^{-1} \mathbf{B}$.
 2. The conduction term must be multiplied by a pre-factor $\varepsilon_{\text{R}}^f l^2$.

Both changes can also be done through the user subroutine “UMATHT.”

- Lastly, the source term needs to be $r = 2(1-d)J^{-1} \mathcal{H}_{\text{R}} - J^{-1} \varepsilon_{\text{R}}^f d$, which can be directly achieved through the “RPL” functionality in the user subroutine “UMAT.”

Before proceeding, we present the UMATHT subroutine as provided in Abaqus/Standard (2024) documentation for completeness.

```

1 SUBROUTINE UMATHT(U,DUDT,DUDG,FLUX,DFDT,DFDG,
2   1 STATEV,TEMP,DTEMP,DTEMDX,TIME,DTIME,PREDEF,DPRED,
3   2 CMNAME,NTGRD,NSTATV,PROPS,NPROPS,COORDS,PNEWDT,
4   3 NOEL,NPT,LAYER,KSPT,KSTEP,KINC)
5 C
6   INCLUDE 'ABA_PARAM.INC'
7 C
8   CHARACTER*80 CMNAME
9   DIMENSION DUDG(NTGRD),FLUX(NTGRD),DFDT(NTGRD),
10  1 DFDG(NTGRD,NTGRD),STATEV(NSTATV),DTEMDX(NTGRD),
11  2 TIME(2),PREDEF(1),DPRED(1),PROPS(NPROPS),COORDS(3)
12 C
13   COND = PROPS(1)
14   SPECHT = PROPS(2)
15 C
16   DUDT = SPECHT

```

```

17     DU = DUDT*DTEMP
18     U = U+DU
19 C
20     DO I=1, NTGRD
21         FLUX(I) = -COND*DTEM DX(I)
22         DFDG(I,I) = -COND
23     END DO
24 C
25     RETURN
26     END

```

Here, we note that “SPECHT,” first introduced in line 14 of the original code, represents the specific heat C listed in Table 1 such that “SPECHT = C .” Similarly, “FLUX,” appearing in line 21 of the original code, represents the heat flux computed using Fourier’s law, following the constitutive relation “FLUX= $-\mathbf{K}\text{grad}\theta$ ” also provided in Table 1.

In what follows, we refer to the original code provided by Abaqus documentation as “original code” and the modifications done in this work as “modified code.”

A.1 Transient term

One could easily impose the equality $\rho C = J^{-1}\zeta_R$ through UMATHT by

1. Prescribing a density $\rho = \zeta_R$ and a specific heat $C = 1$ through the input file, so that $\rho C = \zeta_R$.
2. Passing $J = \det \mathbf{F}$ as a state variable (STATEV) from the UMAT subroutine and modifying line 16 in the original code such that

- original code:

```

16     DUDT = SPECHT

```

- modified code:

```

16     DUDT = SPECHT/detF

```

A.2 Conduction term

Two modifications are needed for the conduction term:

1. To replace the thermal conductivity tensor \mathbf{K} in Fourier’s law by $J^{-1}\mathbf{B}$, we pass \mathbf{F} as a state variable (STATEV) from the UMAT subroutine, which can then be used to calculate $J^{-1}\mathbf{B}$.
2. Moreover, we introduce a pre-factor $\varepsilon_R^f l^2$, referred to as “AUX”, in the code and multiply the conduction term by it.

Both changes are reflected in the code below:

- original code:

```

20     DO I=1, NTGRD
21         FLUX(I) = -COND*DTEM DX(I)
22         DFDG(I,I) = -COND
23     END DO

```

- modified code:

```

20     AUX = (erff*(1c**two))
21     FLUX = zero
22     DO J=1, NTGRD
23         DO I=1, NTGRD
24             FLUX(I) = FLUX(I) - (B(I,J)/detF)*DTEM DX(J)
25         END DO
26     END DO
27     FLUX = FLUX * AUX
28 C
29     DFDG = ZERO
30     DO I=1, NTGRD
31         DO J=1, NTGRD
32             DFDG(I,J) = DFDG(I,J) - (B(I,J)/detF)
33         END DO
34     END DO
35     DFDG = AUX * DFDG

```

A.3 Source term

Lastly, the source term

$$r = 2(1 - d)J^{-1}\mathcal{H}_R - J^{-1}\varepsilon_R^f d$$

can be implemented through RPL in the UMAT subroutine with the details provided in the code (see supplemental materials).

And, since DRPLDT ($\frac{\partial r}{\partial \theta} = \frac{\partial r}{\partial d}$), the variation of RPL with respect to temperature (damage) is needed for the Newton solver to ensure convergence in coupled temperature (damage) - displacement analyses, we also introduce

$$\frac{\partial r}{\partial d} = -2\mathcal{H}_R - \varepsilon_R^f. \quad (31)$$

Remark. At first glance, (31) appears to be missing J^{-1} . However, we encountered convergence issues when using an exact definition that includes J^{-1} , and thus, we have adopted (31) throughout this work.

B Additional constitutive details

In this appendix, we provide the additional constitutive details used in solving the boundary value problems.

B.1 Compressible Neo-Hookean solid

Following Lee et al. (2023), we take the free energy of the undamaged body such that

$$\hat{\psi}_{\mathbf{R}}^0(\mathbf{C}) = \frac{G}{2} [\text{tr}(\mathbf{C}) - 3] + \frac{G}{\beta} [(\det \mathbf{F})^{-\beta} - 1], \quad (32)$$

where G represents the shear modulus, $\beta \stackrel{\text{def}}{=} \frac{2\nu_{\text{poi}}}{1-2\nu_{\text{poi}}}$, with ν_{poi} representing Poisson's ratio. Next, the Cauchy stress can be obtained using (6), (8), and (32) such that

$$\begin{aligned} \mathbf{T} &= J^{-1} \mathbf{F} \left(2 \frac{\partial \hat{\psi}_{\mathbf{R}}^*}{\partial \mathbf{C}} \right) \mathbf{F}^{\top} \\ &= J^{-1} (1-d)^2 [G(\mathbf{B} - (\det F)^{-\beta} \mathbf{1})], \end{aligned} \quad (33)$$

with parameters tabulated in Table 2.

Deformation		Damage	
Parameter	Value	Parameter	Value
G (MPa)	5	$\varepsilon_{\mathbf{R}}^f$ (MPa)	240
ν_{poi}	0.45	l (mm)	0.03
		$\zeta_{\mathbf{R}}$ (MPa s)	0.001

Table 2: Deformation and damage material parameters for a representative compressible Neo-Hookean solid.

B.2 Linear elastic solid

We introduce the Green strain tensor

$$\mathbb{E} = \frac{1}{2}(\mathbf{C} - \mathbf{1}), \quad (34)$$

along with the displacement gradient

$$\mathbf{H} = \mathbf{F} - \mathbf{1}, \quad (35)$$

and use it to recast (34) so that

$$\mathbb{E} = \frac{1}{2}(\mathbf{H} + \mathbf{H}^{\top} + \mathbf{H}\mathbf{H}^{\top}). \quad (36)$$

And since we focus our attention on small deformations (or small strains), we drop the higher order terms in (36) to obtain

$$\mathbb{E} = \frac{1}{2}(\mathbf{H} + \mathbf{H}^{\top}), \quad (37)$$

and take the elastic free energy of the undamaged body such that

$$\hat{\psi}_{\mathbf{R}}^0(\mathbb{E}) = G|\mathbb{E}_0|^2 + \frac{1}{2}K(\text{tr } \mathbb{E})^2, \quad (38)$$

where

$$G \stackrel{\text{def}}{=} \frac{E}{2(1 + \nu_{\text{poi}})}, \quad (39)$$

is the shear modulus, and

$$K \stackrel{\text{def}}{=} \frac{E}{3(1 - 2\nu_{\text{poi}})}, \quad (40)$$

is the bulk modulus. Next, the Cauchy stress can be obtained using (6), (8), and (38) such that

$$\mathbf{T} = \frac{\partial \hat{\psi}_{\mathbf{R}}^*}{\partial \mathbb{E}^e} = (1 - d)^2 [2G\mathbb{E}_0^e + K(\text{tr } \mathbb{E}^e)\mathbf{1}], \quad (41)$$

with parameters tabulated in Table 3.

Deformation		Damage	
Parameter	Value	Parameter	Value
E (MPa)	210000	$\varepsilon_{\mathbf{R}}^f$ (MPa)	20.7
ν_{poi}	0.3	l (mm)	0.03
		$\zeta_{\mathbf{R}}$ (MPa s)	0.001

Table 3: Deformation and damage material parameters for a representative linear elastic solid.

B.3 Large deformation rate-dependent plasticity

We assume in this example that damage nucleates only after the energy exceeds a critical value ψ_{cr} , and that damage initiation and propagation can only occur under tensile loading. Accordingly, (17) is modified as follows

$$\mathcal{H}_{\mathbf{R}}(t) = \begin{cases} \max_{s \in [0, t]} \langle \hat{\psi}_{\mathbf{R}}^0(\mathbf{C}(s)) - \psi_{\text{cr}} \rangle & \text{if } J > 1 \\ \mathcal{H}_{\mathbf{R}}(t - 1) & \text{if } J \leq 1, \end{cases} \quad (42)$$

where $\langle \bullet \rangle$ correspond to the Macaulay brackets and $\mathcal{H}_{\mathbf{R}}(t - 1)$ to the history function in the prior step. Such a formulation allows damage to nucleate only after a critical energy threshold is reached, while preventing damage under compressive loading.⁵

Next, following the previous work of Anand and co-workers (Anand et al., 2009; Srivastava et al., 2010), we revisit (1), and introduce the velocity gradient \mathbf{L}

$$\mathbf{F} = \nabla \chi, \quad \mathbf{L} = \text{grad } \mathbf{v} = \dot{\mathbf{F}}\mathbf{F}^{-1}. \quad (43)$$

⁵Other successful formulations for preventing damage under compressive loadings, such as the volumetric-deviatoric split (Amor et al., 2009) and the spectral decomposition Miehe et al. (2010b) have been reported in the literature.

Moving forward, we adopt the standard multiplicative decomposition

$$\mathbf{F} = \mathbf{F}^e \mathbf{F}^p, \quad \text{with} \quad \det \mathbf{F}^e > 0 \quad \text{and} \quad \det \mathbf{F}^p > 0, \quad (44)$$

of the deformation gradient \mathbf{F} into elastic \mathbf{F}^e and plastic \mathbf{F}^p parts. With (43) and (44), we write the velocity gradient as

$$\mathbf{L} = \dot{\mathbf{F}}\mathbf{F}^{-1} = \mathbf{L}^e + \mathbf{F}^e \mathbf{L}^p \mathbf{F}^{e-1} \quad (45)$$

where

$$\mathbf{L}^e = \dot{\mathbf{F}}^e \mathbf{F}^{e-1}, \quad \text{and} \quad \mathbf{L}^p = \dot{\mathbf{F}}^p \mathbf{F}^{p-1}, \quad (46)$$

are the elastic and plastic velocity gradients, respectively. We also introduce the corresponding elastic and plastic stretching and spin tensors for completeness, such that

$$\begin{aligned} \mathbf{D} &= \text{sym } \mathbf{L}, & \mathbf{W} &= \text{skw } \mathbf{L}, \\ \mathbf{D}^e &= \text{sym } \mathbf{L}^e, & \mathbf{W}^e &= \text{skw } \mathbf{L}^e, \\ \mathbf{D}^p &= \text{sym } \mathbf{L}^p, & \mathbf{W}^p &= \text{skw } \mathbf{L}^p, \end{aligned} \quad (47)$$

with $\mathbf{L} = \mathbf{D} + \mathbf{W}$, $\mathbf{L}^e = \mathbf{D}^e + \mathbf{W}^e$, and $\mathbf{L}^p = \mathbf{D}^p + \mathbf{W}^p$. Further, since assuming an isotropic response, the plastic flow is taken to be irrotational such that

$$\mathbf{W}^p = \mathbf{0}. \quad (48)$$

As a consequence, $\mathbf{L}^p = \mathbf{D}^p$, and

$$\dot{\mathbf{F}}^p = \mathbf{D}^p \mathbf{F}^p. \quad (49)$$

And lastly, plastic flow is assumed to be incompressible such that

$$J^p = 1, \quad (50)$$

and as a result

$$\text{tr} \mathbf{L}^p = \text{tr} \mathbf{D}^p = 0, \quad (51)$$

and therefore

$$J^e = J. \quad (52)$$

We pick the standard form of the free energy *per unit intermediate volume*

$$\psi^e(\mathbf{E}) = G|\mathbf{E}_0^e|^2 + \frac{1}{2}K(\text{tr} \mathbf{E}^e)^2, \quad (53)$$

where G and K are the shear and bulk moduli, given in (39) and (40), respectively, and \mathbf{E}_0^e is the deviatoric part of the logarithmic elastic strain $\mathbf{E}^e = \ln \mathbf{U}^e$.

Following Narayan and Anand (2021), we take the undamaged energy *per unit reference volume* such that

$$\hat{\psi}_R^0(\mathbf{E}) = J^p \psi^e(\mathbf{E}) = \psi^e(\mathbf{E}). \quad (54)$$

Next, the corresponding Mandel stress can be obtained using (6), (8), (53), and (54) such that

$$\mathbf{M}^e = \frac{\partial \hat{\psi}_R^*}{\partial \mathbf{E}^e} = (1-d)^2 [2G\mathbf{E}_0^e + K(\text{tr} \mathbf{E}^e)\mathbf{1}]. \quad (55)$$

We focus our attention on isotropic materials, hence, the corresponding Cauchy stress is related to the Mandel stress by

$$\mathbf{T} \stackrel{\text{def}}{=} J^{-1} \mathbf{R}^e \mathbf{M}^e \mathbf{R}^{e\top}. \quad (56)$$

Now, keeping (44) and (49) in mind, we write the flow rule in the shear-driven form

$$\mathbf{D}^p = \sqrt{\frac{1}{2}} \nu^p \mathbf{N}^p, \quad (57)$$

where ν^p and \mathbf{N}^p are the equivalent plastic shear strain rate and the direction of plastic flow, respectively, and are given by

$$\nu^p = \nu_0 \left(\frac{\bar{\tau}}{(1-d)^2 S} \right)^{1/m}, \quad (58)$$

and

$$\mathbf{N}^p = \frac{\mathbf{M}_0^e}{\sqrt{2\bar{\tau}}}, \quad (59)$$

where \mathbf{M}_0^e is the deviator of the Mandel stress. Moreover,

$$\bar{\tau} \stackrel{\text{def}}{=} \sqrt{\frac{1}{2} \mathbf{M}_0^e : \mathbf{M}_0^e}, \quad (60)$$

is defined as the equivalent shear stress, and S is the deformation resistance. The evolution equation of the deformation resistance is taken to follow

$$\dot{S} = h(S_{\text{sat}} - S)\nu^p, \quad S(\mathbf{x}, t = 0) = S_0, \quad (61)$$

where h , S_{sat} , and S_0 represent the hardening slope, the saturation level of the deformation resistance, and the initial yield strength, respectively. Lastly, material parameters are tabulated in Table 4.

Deformation		Damage	
Parameter	Value	Parameter	Value
E (MPa)	210000	ε_{R}^f (MPa)	5
ν_{poi}	0.3	l (mm)	0.1
ν_0 (1/s)	10^{-4}	ζ_{R} (MPa s)	0.001
m	0.05	ψ_{cr} (MPa)	9
h	5		
S_{sat} (MPa)	450		
S_0 (MPa)	300		

Table 4: Deformation and damage material parameters for a representative rate-dependent plastic solid undergoing large deformation.